ADVANCED MATERIALS
www.advmat.de

An Elastomeric Electrolyte Based on Lithium-Ion-Selective Transmembrane Transport for Solid-State Lithium-Sulfur Batteries

Yifan Zhang, Chao Ding, Jianlong Ding, Jin Chen, Wenqiang Wang, Gengchao Wang,* and Chunzhong Li*

Solid-state lithium-sulfur batteries (SSLSBs) exhibit advantages such as high specific energy, safety, and low cost, making them an ideal candidate for next-generation batteries. However, the current mechanical and electrochemical properties of solid-state electrolytes do not meet the requirements of the practical application of SSLSBs. Herein, a construction strategy of fiber-network-based elastomeric solid electrolytes (FESE) based on electrospinning-induced phase separation is proposed. The FESE features a structure in which an elastomeric layer with Li^+-selective permeability encapsulates a fibrous plastic crystal electrolyte (PCE). This structure originates from the phase separation and fiberization of a hydrogenated nitrile rubber (HNBR) stabilized emulsion, driven by electrostatic jetting. Subsequently, in situ polymerization of methoxy polyethylene glycol is performed within the battery to achieve void filling. Benefiting from the interconnected ion transport channels, the Li^+-selectivity, and the conformal interface, the as-prepared FESE electrolyte achieves a high room-temperature ionic conductivity of 1.11 mS cm^{-1} and a Li^+ transference number of 0.77. The as-assembled SSLSB delivers a high initial discharge capacity (1188 mAh g^{-1}), remarkable rate capability (356 mAh g^{-1} at 4C), and excellent cycling performance (71.2% capacity retention after 800 cycles). This research presents a constructive strategy for the elastomeric electrolytes for high-performance solid-state batteries.

1. Introduction

Solid-state lithium-sulfur batteries (SSLSBs), as a next-generation solution for high-specific energy and high-safety electrochemical energy storage technology, have attracted significant attention in specialized fields such as low-altitude economy, aerospace, and deep-sea exploration.[1–3] Solid-state electrolytes (SSEs) are the core components of SSLSBs.[4] The complete replacement of liquid electrolytes with SSEs not only greatly enhances safety, but also holds the potential to fully address the shuttle effect that has plagued traditional lithium-sulfur batteries.[5–7] Among them, polymer-based solid electrolytes (PSEs) have attracted extensive research interest due to their advantages such as flexibility, excellent interfacial compatibility, and suitability for roll-to-roll manufacturing processes.[8–10] In recent years, researchers have devoted considerable efforts to the meticulous design of PSEs.[11] For instance, the performance of the ion transport domain in PSEs is enhanced by block copolymerization,[12–15] cross-linking,[16] or ion coordination.[17] Furthermore, composite fillers are introduced to construct additional ion-conductive pathways.[18–21] However, these PSEs still fail to balance sufficient ionic conductivity (10^{-4}–10^{-2} S cm^{-1}) and the necessary elastic resilience to accommodate repeated volume changes of the electrodes.[22–24]

Rubber is a class of polymeric materials composed of an amorphous phase in which flexible polymer chains are interconnected by crosslinking zones.[25] By introducing lithium-ion (Li^+) conductive components into rubber elastomers and forming a continuous network, it holds significant potential to develop PSE that simultaneously exhibit ionic conductivity and mechanical robustness, termed elastomeric solid electrolytes (ESEs). Lee et al. developed an elastomeric electrolyte by blending butyl acrylate, a crosslinking agent, and a plastic crystal electrolyte, followed by polymerization-induced phase separation.[26] Due to the formation of a composite structure featuring a thin poly(butyl acrylate) layer encapsulating a 3D interconnected plastic crystal phase, this electrolyte achieved an extremely high room-temperature ionic

Y. Zhang, C. Ding, J. Ding, W. Wang, G. Wang
Shanghai Engineering Research Center of Hierarchical Nanomaterials, Shanghai Key Laboratory of Advanced Polymeric Materials, School of Materials Science and Engineering
East China University of Science and Technology
Shanghai 200237, China
E-mail: wangwenqiang@ecust.edu.cn; gengchaow@ecust.edu.cn

J. Chen
Cell Development Department
SVOLT Energy Technology (Wuxi) Co., Ltd
Wuxi 214000, China

C. Li
Shanghai Engineering Research Center of Hierarchical Nanomaterials, School of Chemical Engineering
East China University of Science and Technology
Shanghai 200237, China

The ORCID identification number(s) for the author(s) of this article can be found under https://doi.org/10.1002/adma.202507331

DOI: 10.1002/adma.202507331

conductivity. However, relying solely on a random distribution of the two phases through simple mixing neither ensures the formation of continuous plastic-crystal-based ion transport channels nor achieves complete encapsulation of the plastic crystal molecules (the SEI additives are further required to prevent the corrosion of lithium by succinonitrile).[27,28] Electrospinning is a polymeric material fabrication technique that utilizes a high-voltage electric field to align molecular chains, thereby forming jets and fiberization.[29,30] If the phase separation-curing of ESEs can be coupled with the fiberization via electrospinning, it would be highly beneficial for the formation of highly interconnected ion transport channels and the full utilization of the elastic resilience of the rubber matrix.

Herein, we report for the first time a construction strategy of fiber-network-based elastomeric solid electrolytes (FESE) based on electrospinning-induced phase separation. The prepared FESE exhibits a vascular-like structure, where fibrous plastic crystal electrolyte (PCE) is encapsulated by elastomeric layers capable of selectively permeating Li^+. This structure originates from the phase separation and fiberization of a hydrogenated nitrile rubber (HNBR) stabilized emulsion, driven by electrostatic jetting. The obtained fibrous membrane achieves a tensile strength of 5.9 MPa and a breaking elongation of 313%. Subsequently, in situ polymerization of methoxy polyethylene glycol (*m*PEG) within the battery is performed to achieve void filling and intimate contact between the electrolyte and the electrodes. Benefiting from the interconnected ion transport channels of the PCE phase, the Li^+-selectivity of the HNBR encapsulation layer, and the conformal interface formed by in situ polymerization, the as-prepared FESE exhibits a high room-temperature ionic conductivity of 1.11 mS cm^{-1} and a Li^+ transference number of 0.77. The as-assembled SSLSB demonstrates a high initial discharge capacity (1188 mAh g^{-1} at 0.1C), remarkable rate capability (356 mAh g^{-1} at 4C), and excellent cycling performance (71.2% capacity retention after 800 cycles at 1C).

2. Results and Discussion

The design concept of the FESE is illustrated in **Figure 1a**. Our strategy is accomplished through three main steps, namely, emulsion formation, fiberization, and interfacial conformality. 1) The molecular chain of HNBR is composed of polyolefin segments (retaining a certain double bond) and polyacrylonitrile segments. Due to the significant difference in polarity between these two segments (reflected in their distinct solubility parameters, with polyolefin at 16–19 $J^{1/2}$ $m^{-3/2}$ and polyacrylonitrile at 25.3 $J^{1/2}$ $m^{-3/2}$),[31,32] the HNBR exhibits quasi-surface-active effects. By adding the PCE (succinonitrile and lithium salts) into a xylene solution (containing dissolved HNBR) and applying high-speed homogenization, a stable emulsion can be obtained. In the case of emulsion particles, the strong interactions among polar nitrile groups cause the polyacrylonitrile chains of HNBR to stretch into the PCE phase. Meanwhile, the polyolefin segments tend to orient toward the non-polar solvent side, thereby forming an emulsion in which an outer HNBR phase stabilizes the inner PCE phase. 2) During the electrospinning process, the emulsion forms jets under the electrostatic force, and the emulsion particles within are stretched and fused with each other. As the solvent gradually evaporates, the non-polar chain-enriched region on the outer layer undergoes saturated phase separation and simultaneous UV crosslinking to form an HNBR skin layer. A fiber-network-based elastomeric solid membrane (FESM) with the HNBR sheath and the PCE core is obtained. 3) To fill the voids between the fibers of FESM and achieve good interfacial contact with the electrodes, the *m*PEG is in situ polymerized to obtain the fiber-network-based elastomeric solid electrolytes (FESE).

In the system design of this work, the differential affinity of the polar polyacrylonitrile segments and non-polar polyolefin segments in the HNBR toward the PCE phase is essential for the formation of the emulsion and the fiber encapsulation layer. Density functional theory (DFT) structural optimization and calculations reveal a significant difference in the binding energy of polyacrylonitrile segments and polyolefin segments to succinonitrile (SN), with values of −0.19 and 0.07 eV, respectively. This indicates that the polar polyacrylonitrile segments of HNBR exhibit a spontaneous affinity for SN, while its nonpolar polyolefin segments demonstrate repulsion toward SN. It is also found that the polyacrylonitrile segments of the HNBR exhibit a binding energy of −1.19 eV with LiTFSI, which is comparable to the binding energy of SN with LiTFSI (−1.26 eV). This suggests that the polyacrylonitrile segments also make a significant contribution to the solvation of lithium salts (Figure 1b; Figure S1, Supporting Information).

To further explore the manifestations of the aforementioned intermolecular affinity and repulsion in a macroscopic system, the morphology and stability of the emulsion are investigated. In the optical microscopy image of the emulsion (Figure 1c), the emulsion particles are spherical in shape and exhibit relatively uniform particle sizes, and the particle size distribution indicates a particle size of ≈0.7–2 µm. After the emulsions or dispersions formed by adding polymers of different polarity are left standing for 24 h, it is found that the HNBR-stabilized emulsion maintained excellent dispersibility (Figure S2, Supporting Information). In contrast, the dispersion formed by the addition of non-polar polyolefin elastomer (POE) undergoes phase separation, leading to stratification. Meanwhile, the dispersion formed by the addition of polar polyacrylonitrile results in sedimentation caused by the flocculation. This proves that the amphiphilic nature of HNBR plays a critical role in maintaining a stable spherical PCE emulsion. In addition, the substitution of HNBR with ethylene-vinyl acetate copolymer (EVA) or SN with N-methylacetamide (NMA) yields similar emulsions (Figures S3 and S4, Supporting Information). The universality of amphiphilic polymers in stabilizing emulsions is demonstrated. The process and formation mechanism of fiberizing emulsions to prepare the FESM require attention. The phase field simulation based on three-phase flow (Figure 1d) simulates this process: initially, the emulsion particles undergo electro-coalescence under an electric field, promoting the merging of emulsion particles. The coalesced emulsion is then stretched and generates electrostatic jets under a high-voltage electric field, leading to the fiberization of the emulsion. The HNBR phase initially coats the outer surface of the emulsion particles and also forms an encapsulating layer during the fiberization process.

Figure 2a illustrates the apparatus we designed for electrospinning and simultaneous UV crosslinking. The simultaneous UV crosslinking enables the timely crosslinking of polyolefin segments with a small number of unsaturated bonds in the HNBR

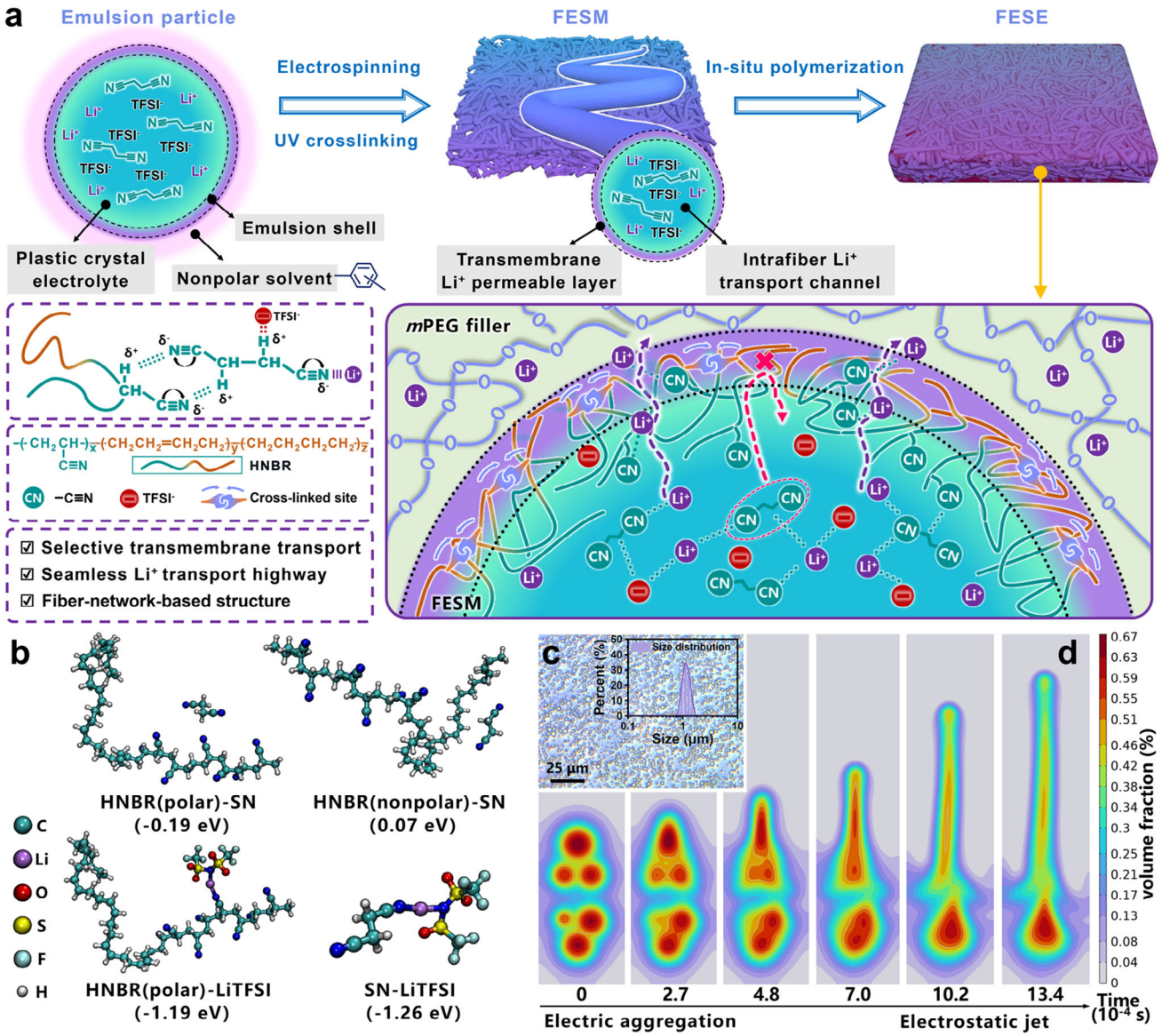

Figure 1. a) Schematic diagram of the preparation process and ion transport mechanism of FESE. b) Binding energies of HNBR (polar)-SN, HNBR (nonpolar)-SN, HNBR (polar)-LiTFSI, SN-LiTFSI. c) Optical microscope image and particle size distribution of the HNBR-xylene/SN-LiTFSI emulsion. d) Three-phase flow simulation: the formation of FESM fibers with the electrostatic jet of the HNBR-xylene/SN-LiTFSI emulsion.

encapsulation layer, thereby effectively solidifying the fibers obtained from electrospinning. This prevents the structural damage caused by thermal motion. The FESM obtained through electrospinning, as shown in Figure 2b, exhibits advantages such as thinness and elasticity. Due to its capability for continuous production, it holds potential for application in roll-to-roll processes. To prepare high-performance ion-conducting fibers via electrospinning-induced phase separation, we optimize various parameters including solid content, voltage, temperature, and emulsion feed ratio (HNBR: PCE). We observe that when the HNBR solution concentration is too low or the temperature is too low, the fiber membrane exhibits discontinuous fibers with bead-like structures (Figures S5 and S6, Supporting Information). Conversely, when these two are too high, the fibers exhibit adhesion and collapse. Moreover, A high voltage facilitates sufficient stretching of the emulsion in the electric field (Figure S7, Supporting Information). Ultimately, we select a concentration of ≈10%, a temperature range of 20–30 °C, a voltage of 24 kV, and a critical HNBR/PCE ratio of 2:8 (Figure S8, Supporting Information).

The final optimized FESM shows a 3D interconnected structure formed by the overlapping and fusion of fibers (Figure 2c). This can be attributed to the fact that complete solvent evaporation and sufficient UV crosslinking require a certain amount of time. During this time, the chain segments in the fiber encapsulation layer retain good mobility, leading to a tendency for mutual fusion. Besides, the electrospinning-induced phase separation exhibits broad applicability to other amphiphilic polymers

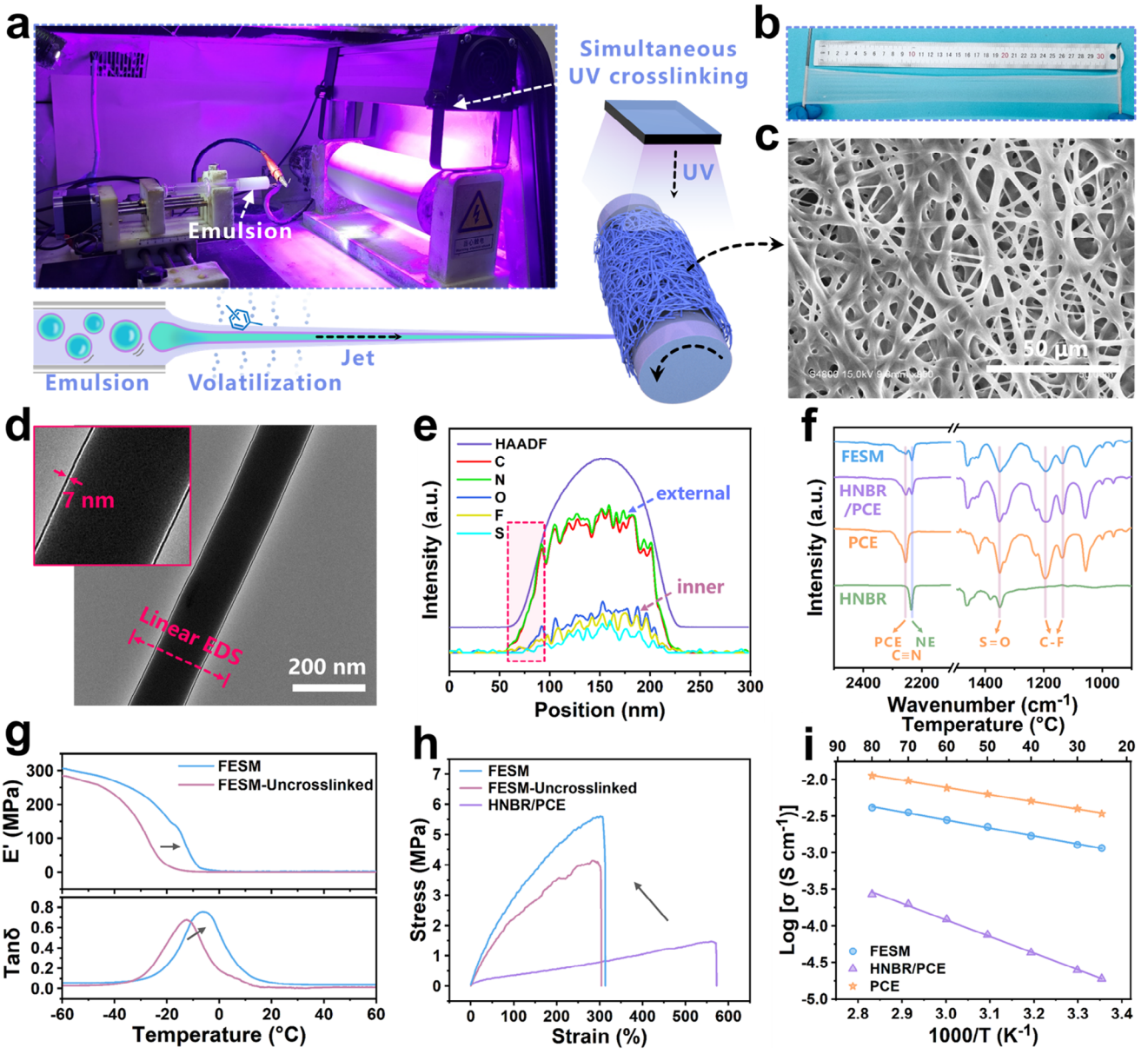

Figure 2. a) Apparatus exhibition and schematic diagram of the electrospinning and in situ crosslinking of FESM. b) Digital photo of the FESM. c) FESEM image of the FESM. d) HRTEM image and e) corresponding EDS line scanning of C, N O, F, and S for a single FESM fiber. f) FTIR spectra of FESM and HNBR/PCE blend membrane. g) DMA curves of HNBR and FESM before and after UV crosslinking. h) Stress–strain curves of the HNBR and the FESM before and after UV crosslinking. i) Ion conductivity-temperature curves of the FESM, HNBR/PCE blend membrane, and PCE.

(e.g., EVA, Figure S9, Supporting Information). Beyond that, the high-resolution transmission electron microscopy (HRTEM) image of a single fiber of FESM is further shown in Figure 2d. The fiber exhibits uniform thickness, with a diameter of ≈164 nm. A black outline with a thickness of ≈7 nm is observed on the outer surface of the fiber, which can be attributed to the presence of the encapsulation layer. Based on a geometric model of coaxial cylinders, it can be calculated that the encapsulation layer accounts for ≈28% of the HNBR mass in the feed. It is inferred that the remaining portion of HNBR extends into the PCE phase and composites with it. Furthermore, the EDS line scanning results along the radial direction of the fiber (Figure 2e; Figure S10, Supporting Information) reveal that the characteristic elements of the material system (C, N, O, F, S) all exhibit a trend of higher intensity in the center and gradually decreasing toward the sides, which is typical of the peak-shaped radial response of fiber materials. However, the signal intensities of O, F, and S, originating solely from LiTFSI, are significantly lower than those of C and N, and the distribution widths of these signals are also narrower. This implies that the PCE phase containing LiTFSI is encapsulated within the encapsulation layer.

To further reveal the core-shell structure of FESM, the FTIR analysis is adopted. In contrast, an HNBR/PCE blend membrane with the same feeding ratio as FESM is prepared. In the FTIR

spectra (Figure 2f), the peak intensity of FESM at 2236 cm^{-1}, corresponding to the stretching vibration of —C≡N in HNBR, is similar to that of the HNBR/PCE blend membrane.[33] However, the peak intensity of FESM at 2255 cm^{-1}, corresponding to the stretching vibration of C≡N in SN, is significantly weaker than that of the HNBR/PCE blend membrane. This implies that the PCE phase is encapsulated inside the FESM fibers by HNBR. This innovative fiber encapsulation design not only effectively stabilizes the PCE phase but also significantly suppresses the migration of SN and lithium salt anions. In addition, the peaks of FESM at 1138 and 1202 cm^{-1}, corresponding to the C—F bond in LiTFSI, are weaker compared to the HNBR/PCE, further supporting this observation.[34]

In order to evaluate the crosslinking effect of UV, DMA testing is employed. After UV irradiation, the storage modulus and the peak temperature of Tanδ (i.e., Tg) of the FESM increase (Figure 2g). This can be attributed to the cross-linking of the polyolefin segments with a small number of unsaturated bonds in the outer layer of the fibers. Subsequently, based on the calculation of cross-linking density using the formula $\nu_e = E_s/3RT$, where E_s represents the plateau storage modulus above Tg (T = Tg + 40 + 273.15 K) and R is the gas constant.[35] The ν_e of FESM increases from 61 to 94 mol m^{-3}. This further indicates the effective cross-linking of the polyolefin segments in the outer layer, thereby enhancing the mechanical and thermal stability of the fiber structure. Moreover, the stress–strain curves of the different membranes are shown in Figure 2h. The tensile strength of the HNBR/PCE blend membrane is only 1.3 MPa. For the uncrosslinked FESM, the oriented structure induced by electrospinning significantly enhances the tensile strength to 4.1 MPa. Although the elongation at the break of the FESM decreases, it still achieves an excellent value of 307%. After UV cross-linking, the tensile strength of the FESM further increases to 5.9 MPa. And its elongation at break remains almost unchanged (313%). These results demonstrate that the combination of electrospinning and simultaneous UV cross-linking is highly beneficial for obtaining FESM with excellent mechanical properties.

Surprisingly, despite the comprehensive encapsulation of the PCE phase, the FESM still shows a high room-temperature ionic conductivity of 1.08 mS cm^{-1} (Figure 2i; Figure S11, Supporting Information), which fully leverages the ion transport capability of PCE (3.41 mS cm^{-1}). This phenomenon can be attributed to the ultra-thin encapsulation layer of FESM, which likely contains microdomains of nitrile segments that provide a weakly solvating environment sufficient to facilitate Li^+ transport. In contrast, HNBR/PCE demonstrates a significantly lower room-temperature ionic conductivity of only 0.019 mS cm^{-1}. This difference is presumably due to the blocking effect on ion transport caused by the HNBR, particularly the polyolefin phase, within the HNBR/PCE system.

The FESE is obtained by in situ polymerization of *m*PEG to fill the voids of FESM, and its morphology and electrochemical performance are subsequently evaluated. Notably, during the assembly of the SSLSBs, the FESM is in situ electrospun onto the cathode sheet. The fibers conform to the micro-curved surface of the cathode before solidification, thereby enhancing the interfacial mass transfer between the electrolyte and the active material (Figure S12, Supporting Information). It is evident that in situ polymerization provides superior conformal interfacial adhesion, which ensures efficient ion transport at the interface and avoids interfacial failure (Figure S13, Supporting Information). For comparison, a blended elastomeric solid electrolyte (BESE) is prepared by in situ polymerization of *m*PEG using the same formulation ratio as FESE, but with a three-phase mixture of HNBR/PCE/*m*PEG. The composite FESE exhibits a smooth surface while retaining a clear fibrous structure internally (Figure S14, Supporting Information), indicating that the in situ polymerization process does not disrupt the fibrous network of FESE. In contrast, the BESE displays a distinctly segmented and discontinuous structure, where the PCE phases are separated by polymer phases. This potentially leads to the obstruction of Li^+ transport pathways (Figure S15, Supporting Information). Consequently, the FESE exhibits a high room-temperature ionic conductivity of 1.11 mS cm^{-1} (**Figure 3a**; Figure S16, Supporting Information). In contrast, the BESE demonstrates a significantly lower room-temperature ionic conductivity of only 0.0098 mS cm^{-1}. This indicates that the continuous ion transport pathways formed by the fiber network significantly enhance the ionic conductivity of the *m*PEG (0.0026 mS cm^{-1}) compared to random and tortuous channels. When tested at various temperatures, both FESE and BESE show that their conductivity-temperature relationships follow Arrhenius-type behavior, indicating that the Li^+ transport in the PCE phase is dominant. Based on the Arrhenius equation, the activation energy for FESE is calculated to be 0.22 eV, substantially lower than that of BESE (0.53 eV). This can likely be attributed to the continuous PCE phase in FESE, which forms an interconnected ion transport network.

To further compare the differences in Li^+ transport properties caused by the phase structure variations between BESE and FESE, we conduct separate modeling approaches. For BESE, a Turing pattern-like phase separation model is established using the lattice Boltzmann method to generate the fluid phase field (Figure S17, Supporting Information). Subsequently, the ease of ion transport is simulated through finite element analysis based on electric field and ion concentration distributions. Evidently, the polymer continuous phase in BESE disrupts the connectivity between PCE domains, resulting in discontinuous PCE ion transport pathways and a lower ion flux scale (Figure 3b). In contrast, FESE achieves a significantly higher (two orders of magnitude) ion flux scale due to its interconnected fibrous ion transport channels and selective Li^+ permeation capability (Figure 3c). Furthermore, the single ion transport cross-section in FESE exhibits a more uniform ion flux distribution, indicating uniform energy barriers during ion transport. And the fiber fusion points further enhance the ion current density (Figure S18, Supporting Information). In comparison, the ion transport cross-section in BESE shows abrupt transition points, i.e., phase interfaces. Since the electrolyte along the ion pathways exhibits a series resistance effect, the high energy barrier regions in BESE will significantly reduce the overall ion transport capacity of the entire electrolyte. These results verify the conclusion of the conductivity test.

The electrochemical stability of FESE also deserves attention. It can be observed that the FESE exhibits a wide electrochemical stability window of 0.5–5.0 V, which allows reversible cycling in most solid-state battery systems (Figure 3d). In contrast, the electrochemical stability window of conventional PCE and BESE

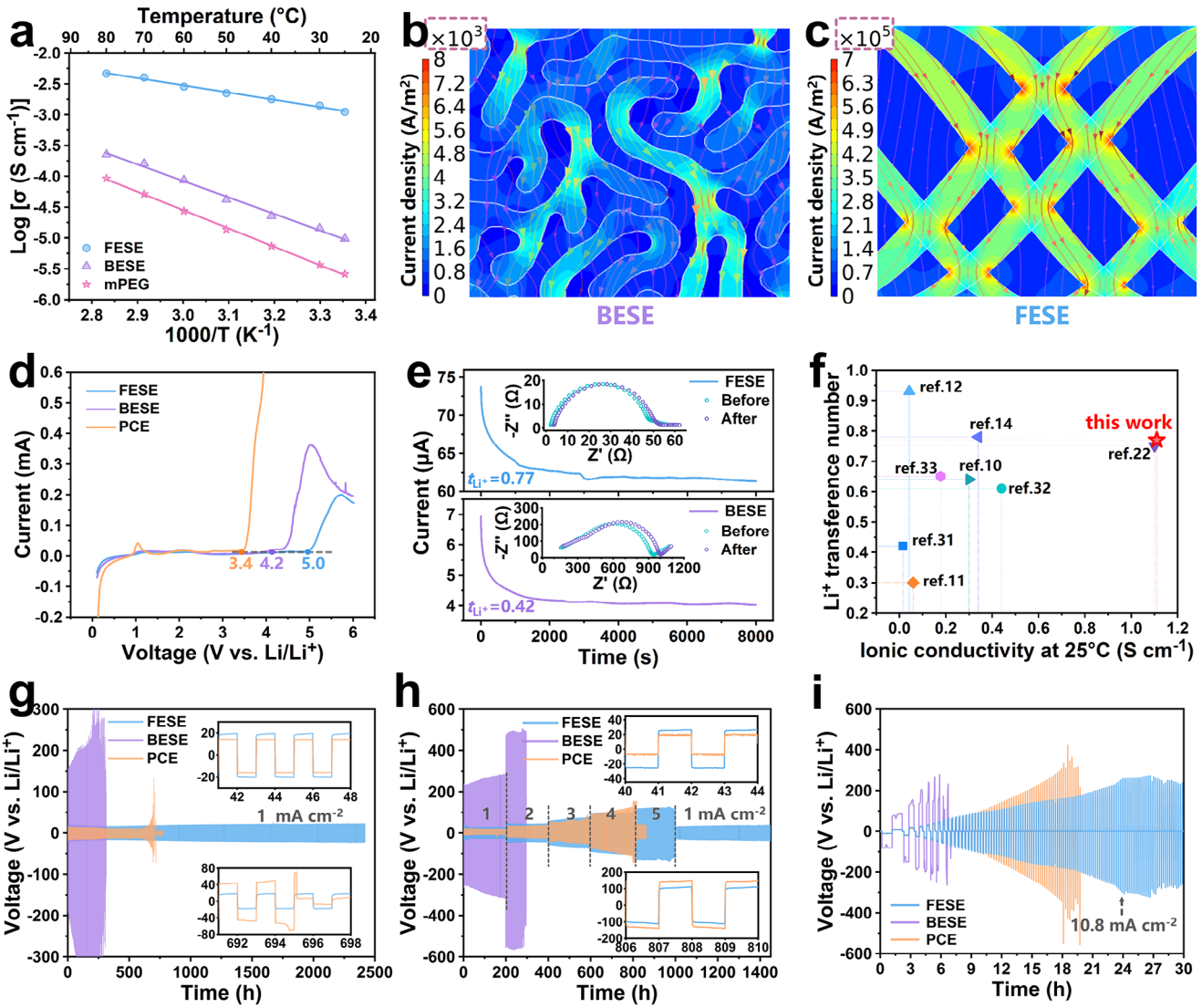

Figure 3. a) Ion conductivity–temperature curves of the FESE, BESE and *m*PEG. Simulation of ion flux concentration during operation of b) BESE and c) FESE. d) LSV profiles of the stainless steel//Li cells with FESE, BESE, and PCE. e) EIS curves before and after the polarization test and the corresponding chronoamperometry (CA) curves with an amplitude of 10 mV for Li//Li symmetric cells equipped with FESE and BESE. f) Comparison of room-temperature ionic conductivity and Li^+ diffusion coefficient between the FESE and other PSEs. g) Galvanostatic cycling curves at 1 mA cm^{-2}, h) Galvanostatic cycling curves from 1 to 5 mA cm^{-2}, and i) Critical current density of the Li//Li symmetric cells equipped with FESE, BESE, and PCE.

are only 1.2–3.4 V and 0.6–4.2 V, respectively. This is because both electrolytes contain freely mobile SN, which leads to irreversible side reactions when in contact with lithium metal. This also shows that the ingenious fiber encapsulation structure and superior mechanical properties of the FESE effectively confine the PCE phase in the core.

The FESE demonstrates a higher Li^+ transference number (t_{Li^+} = 0.77, Figure 3e; Figure S19, Supporting Information) compared to the conventional PCE (t_{Li^+} = 0.37) and BESE (t_{Li^+} = 0.42). This further suggests that the small amount of nitrile groups present on the surface of the HNBR encapsulation layer selectively facilitates Li^+ permeation while restricting anion movement. Such high Li^+-selectivity is crucial for fully utilizing the ion transport network and enabling rapid charge–discharge capabilities in solid-state batteries. In summary, the FESE exhibits significant comprehensive advantages over recently reported PSEs in terms of two key electrolyte metrics: room-temperature ionic conductivity and Li^+ transference number (Figure 3f).[13–15,17,26,36–38]

To further evaluate the Li^+ transport performance, the FESE is assembled into a Li symmetric cell for lithium deposition-stripping tests (Figure 3g,h). At a high current density of 1 mA cm^{-2}, the cell with BESE exhibits fluctuating deposition potentials from the outset. In contrast, the cell with FESE demonstrates excellent and stable cycling performance with low polarization over 2400 h. Specifically, the cell with FESE shows an extremely low polarization of 19 mV at 1 mA cm^{-2}, significantly lower than that of the cell with BESE (93–247 mV) and slightly higher than that of the cell with PCE. However, the cell with PCE failed after only ≈700 h of operation due to the accumulation of dendrites and dead lithium. Furthermore, the cell with FESE maintains

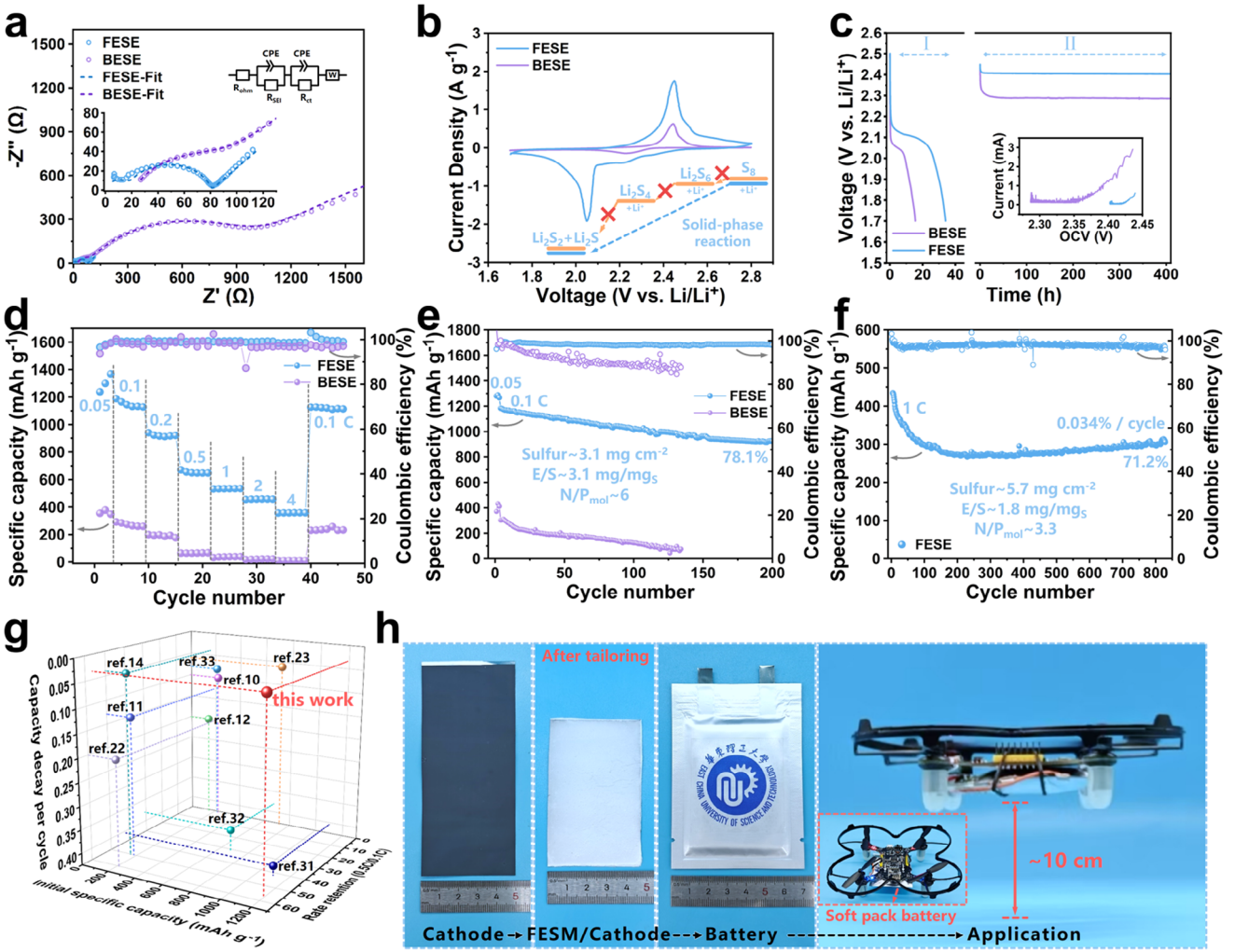

Figure 4. a) Nyquist plots and corresponding equivalent circuit fitting curves, b) CV curves at a scan rate of 0.1 mV s^{-1} (Ladder Diagram: Differences in polysulfide conversion pathways in liquid or solid states), c) voltage variation and corresponding self-discharge current in continuous self-discharge current testing (I: Capacity calibration using low current constant current discharge at C/40, II: Open circuit self-discharge), d) rate performance from 0.1C to 4C, and e) cycling performance at 0.1C of SSLSBs equipped with the FESE or BESE. f) Cycling performance at 1C with high sulfur loading of SSLSB equipped with the FESE. g) Comparison of comprehensive performance between this work and others. h) The S/CNTs cathode, FESM/cathode integrated component, soft pack SSLSB equipped with FESE and its application in unmanned aerial vehicles.

exceptional stability across various current densities ranging from 1 to 5 mA cm^{-2}. Even under prolonged operation or at high current densities, irregular fluctuations at the edges of the deposition potential (typically attributed to the dendrites and dead lithium) are absent (illustrations of Figure 3g,h). The low polarization of FESE can be attributed to its high Li^+ transport capability and the highly adhesive conformal interface with Li metal formed by the in situ process, which significantly reduces Li^+ mass transport resistance and ensures uniform Li^+ flux. Consequently, the FESE demonstrates stable Li^+ transport at a high critical current density of 10.8 mA cm^{-2} in the critical current density test (Figure 3i). Additionally, in Li||Cu asymmetric cells, FESE demonstrates a low nucleation overpotential (35 mV) and an average Coulombic efficiency of 96.4% over 420 cycles (1 mA cm^{-2}, 0.1 mAh cm^{-2}) (Figure S20, Supporting Information). These results highlight the effectiveness of the fiber-encapsulated structure in FESE for enhancing the stability of lithium anodes.

The FESM was in situ electrospun onto the cathode (≈3.1 mg cm^{-2} and S content of 57.1%, Figure S21, Supporting Information), followed by in situ polymerization of *m*PEG, achieving an integrated composite of the electrode and electrolyte in the assembled SSLSB. The electrochemical performance of the assembled SSLSB was evaluated to investigate the impact of FESE on the ion transport and sulfur conversion kinetics. **Figure** 4a shows the Nyquist plots of SSLSBs with FESE and BESE, where the high-frequency region displays a small semicircle and a large semicircle corresponding to the ion transport within the solid electrolyte interphase (SEI) and electrolyte, respectively. An equivalent circuit of $R_{ohm}(RQ)_{SEI}(RQ)_{ct}W$ is selected to fit the Nyquist curves. Here, a resistor element in parallel with a constant phase element (RQ) is used to describe individual non-ideal polarization processes. Specifically, R_{ohm} represents the ohmic resistance, $(RQ)_{SEI}$ represents the ion transport within the SEI, and $(RQ)_{ct}$ represents the ion transport within

the electrolyte. The fitted R_{ct} and R_{SEI} of the SSLSB with FESE are 66.1 and 6.9 Ω, respectively (Table S1, Supporting Information). These values are significantly lower than those of SSLSB with BESE (R_{ct} = 898 Ω and R_{SEI} = 59.7 Ω). This reveals that the SSLSB with FESE exhibits improved ion transport performance due to the continuous PCE phase, as well as enhanced interfacial transport performance through the synergistic effects of in situ electrospinning, in situ polymerization, and flexible interfaces.

To evaluate the impact of the solid-state electrolyte system on sulfur conversion kinetics and pathways, the cyclic voltammetry (CV) tests are measured at a scan rate of 0.1 mV s^{-1} (Figure 4b). Notably, both the oxidation and reduction peaks in the SSLSB with the FESE merge into single peaks (2.45 and 2.04 V) compared to the conventional liquid LSBs. This indicates that FESE selectively confines sulfur species, promoting their solid-phase conversion within the cathodes (i.e., direct conversion between S_8 and short-chain Li_2S_2 and Li_2S).[39] The reduction peak in the 2.05–1.85 V region corresponds to the conversion of S_8 to short-chain Li_2S_2 and Li_2S, which aligns with the charge–discharge curve at 0.1C of the SSLSB with FESE (Figure S22a, Supporting Information). Additionally, the observed discharge curve is similar to those reported for other SSLSBs.[40] In contrast, the SSLSB with BESE exhibits a much smaller CV curve enclosed area due to incomplete S_8 reactions caused by the insufficient Li^+ supply rate. Moreover, the LSB with PCE fails to charge and discharge properly due to the corrosive nature of SN toward lithium (Figure S22b, Supporting Information).

Through the composite confinement of PCE, the FESE, and BESE can limit the contact between PCE and lithium to varying degrees while leveraging the high Li^+ transport capability of PCE to achieve high-performance SSLSBs. The confinement on PCE determines the operational reliability of the lithium anode and SSLSB. The FESE, with its ingenious design, selectively blocks the PCE phase, thereby preventing small molecules from diffusing along the concentration gradient. This is supported by the self-discharge curves and continuous discharge current (Figure 4c). During the continuous self-discharge current test, a small discharge current at C/40 is first applied for capacity calibration to calculate the self-discharge current under open-circuit voltage. Notably, the SSLSB with FESE exhibits a polarization voltage drop only in the initial stage after charging. After 400 h of self-discharge testing, it maintains a high potential of 2.42 V. In contrast, the larger voltage drops and self-discharge current in the SSLSB with BESE are likely attributed to side reactions between leaked plastic crystals and sulfur species dissolved in PCE with the lithium anode.

Owing to its superior Li^+ transport capability and structural design, the SSLSB with FESE exhibits excellent rate performance across a range of current densities of 0.1, 0.2, 0.5, 1, 2, and 4C, delivering capacities of 1188, 940, 670, 531, 454, and 356 mAh g^{-1}, respectively (Figure 4d). At all rates, the SSLSB with FESE maintains significantly higher specific capacities than the SSLSB with BESE, demonstrating that its Li^+ transport capability matches the sulfur species conversion kinetics even at high current densities. After 200 cycles at 0.1C, the SSLSB with FESE retains a high specific capacity of 923 mAh g^{-1}, with a capacity retention of 78.1% (a decay rate of 0.11% per cycle, Figure 4e). In contrast, the SSLSB with BESE retains only 75 mAh g^{-1} after 135 cycles at 0.1C, with a capacity retention of 24.8% (a decay rate of 0.56% per cycle).

In order to achieve a truly viable high-energy-density SSLSB and evaluate the performance of FESE under extreme operating conditions, the SSLSB with FESE is operated under high loading (5.7 mg cm^{-2}) and high-rate (1C) conditions (Figure 4f). Long-term cycling test demonstrates that it maintains a high-capacity retention of 71.2% even after more than 800 cycles. To comprehensively compare our device, we select three metrics including initial specific capacity, rate retention (0.5C/0.1C), and capacity decay per cycle to benchmark against other works.[13–15,17,26,27,36–38] Clearly, our work exhibits the best overall performance and competitive individual metrics (Figure 4g). Moreover, the FESE based on in situ electrospinning and in situ polymerization is fabricated and assembled into a soft pack SSLSB. It shows capacity retention of 77.0% after 100 cycles at a sulfur loading of 2.8 mg cm^{-2} (Figure S22d, Supporting Information). Furthermore, a soft pack SSLSB is assembled using a series configuration of two cathode and anode pairs (Figure S22e, Supporting Information) and successfully powers a small drone for continuous operation (Figure 4h; Video S1, Supporting Information). This has never been achieved in previously reported works of soft-pack SSLSBs.

We further investigate the kinetic processes induced by the solid-phase reaction of sulfur species within the cathode due to the FESE, based on in situ impedance changes and the distribution of relaxation times (DRT) during charge–discharge. Notably, since the constant current charge–discharge process exhibits significant polarization-induced kinetic hysteresis, it is unable to reflect the actual reaction and mass transport processes. So, we employ stepwise potentiostatic charge/discharge at intervals of 0.2 V (with intervals of 0.1 V in kinetic hotspot regions). In DRT analysis, the relaxation time is the time required for electrochemical system variables to transition from a transient state to a near-steady state under external perturbations. The peaks corresponding to different relaxation times in DRT analysis signify distinct reaction kinetic processes. During the SSLSB with FESE operating, three polarization contributions with different time constants are identified. The systematic parameter-dependent analysis supports the following processes: redox reactions within the cathode (P1: 10^{-2}–10^{-1}), interfacial Li^+ transport in the SEI (P2: 10^{-1}–10^{0}), and Li^+ transport in the electrolyte (P3: 10^{0}–10^{1}) (**Figure 5**a–f; Figure S23, Supporting Information). Obviously, the SSLSB with FESE exhibits more stable interfacial and mass transport kinetic responses compared to the SSLSB with BESE, with almost no significant changes observed throughout the charge–discharge process. This explains the superior electrochemical performance and cycling stability of the SSLSBs with FESE. However, for the SSLSB with BESE, the peak values and impedance responses of the P2 and P3 processes (i.e., Li^+ mass transport resistance at the interface and electrolyte) increase significantly with the depth of discharge (Figure 5a,b). This is due to the uneven and blocked PCE phase in the BESE electrolyte, which fails to provide a continuous high-speed Li^+ transport pathway. This results in excessively high Li^+ transport resistance in the P3 process (charge transfer resistance of ≈950 Ω) (Figure 5c). This Li^+ supply rate, mismatched with the demands of redox kinetics, can only satisfy the conversion of sulfur species near the electrolyte. As the discharge depth increases, the gradually decreasing electromotive force becomes insufficient to overcome the increasing mass transport resistance. Consequently, Li^+ cannot be

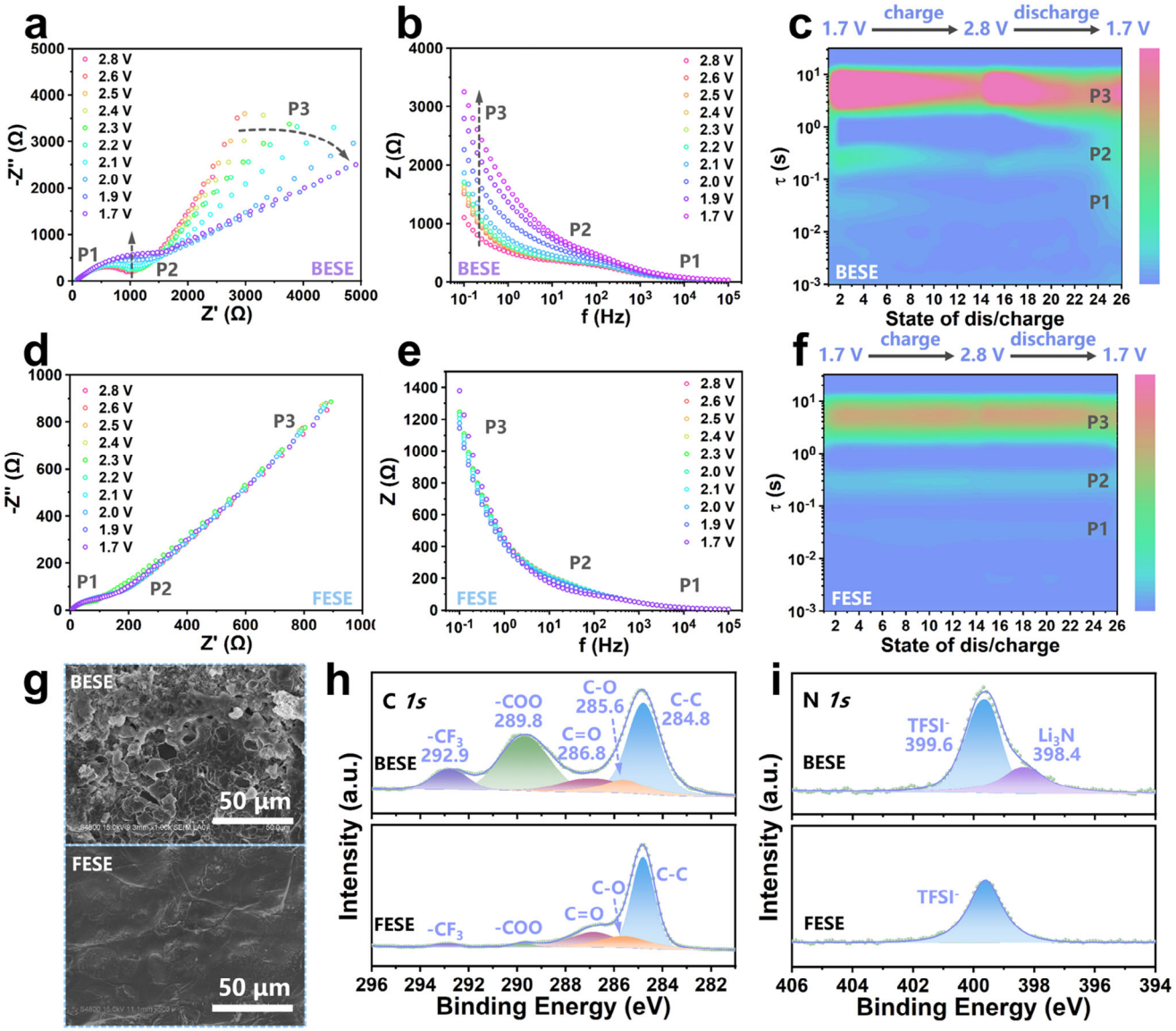

Figure 5. a) In situ Nyquist plots, b) In situ Bode plots, and c) In situ DRT responses of the SSLSBs equipped with the BESE during stepwise potentiostatic charging/discharging. d) In situ Nyquist plots, e) In situ Bode plots, and f) In situ DRT responses of the SSLSBs equipped with the FESE during stepwise potentiostatic charging/discharging. g) Superficial FESEM images, h) C 1s and i) N 1s XPS spectra of the lithium anodes after 50 cycles for SSLSBs equipped with the BESE and FESE.

further driven to participate in the reaction, manifesting as incomplete S_8 conversion and lower capacities. Besides, this unstable Li^+ transport rate also leads to the formation of disordered SEI and dendrites. In contrast, the ingenious Li^+-selectivity and continuous transport channels of FESE ensure consistently low Li^+ transport impedance in the P3 process. Meanwhile, the conformal interface provides stable interfacial Li^+ transport capability in the P2 process (Figure 5d–f). As a result, the supplied Li^+ can meet the efficient in situ conversion of sulfur species throughout the P1 process, leading to excellent overall electrochemical performance.

The surface morphology of the lithium anodes before and after cycling can be used to validate the aforementioned mechanism (Figure 5g). It can be observed that the surface of the pristine lithium anode is smooth and flat (Figure S24, Supporting Information). In the SSLSB with BESE, after dozens of cycles, lithium dendrites densely cover the anode surface. This can be attributed to the random Turing-pattern-type phase distribution in BESE. This is because it neither effectively suppresses the detrimental side reactions between SN and lithium, nor ensures a stable and uniform Li^+ mass transport rate. Conversely, the lithium surface in the SSLSB with FESE remains flat with almost no dendrites, and the SEI is smooth.

The surfaces of the cycled lithium anodes are analyzed by XPS to obtain the bonding information of the SEI components. The C 1s spectra exhibit the peaks corresponding to —CF_3 (292.9 eV), —COO (289.8 eV), C═O (286.8 eV), and C—O (285.6 eV) (Figure 5h). It is found that the intensities of the

—COO peak and the —CF_3 peak in SEI of the SSLSB with FESE are much weaker than that of the SSLSB with BESE. The stronger —COO peak of SSLSB with BESE is ascribed to the formation of alkyl lithium carbonate resulting from the side reactions due to the leakage of SN, which also causes a pitted surface as shown in the aforementioned FESEM image. Such a pitted surface significantly increases the side reaction between exposed lithium and organic components. In contrast, the encapsulation structure of FESE prevents SN from eroding the lithium anode, resulting in a more uniform SEI and fewer side reactions. Similarly, the N 1s spectrum of the SSLSB with BESE displays peaks from $TFSI^-$ (399.6 eV) and Li_3N (398.4 eV), and the Li_3N is the final product of the reaction between the SN and the lithium anode (Figure 5i). Conversely, the N 1s spectrum of SSLSB with FESE does not exhibit the peak corresponding to Li_3N. Although Li_3N is generally a useful component for the SEI, it cannot reverse the intensified side reactions caused by the uneven and eroded lithium surface or mitigate the damage to battery performance. These results demonstrate that the FESE has excellent confinement on SN and significantly protects the lithium anode.

The cycled cathode and FESE are also worth investigating for evaluating the stability of the encapsulation structure. In the SSLSB with FESE, the cathode surface remains dense (Figure S25, Supporting Information), and the cross-sectional FESEM image reveals a uniform sulfur distribution (Figure S26, Supporting Information). In contrast, the cathode surface in the SSLSB with BESE appears rough and porous, with sulfur distribution showing a "high inside, low outside" trend. This is attributed to the erosion and dissolution of sulfur species by leaked PCE in the BESE. The presence of S^{2-} and S_22^- peaks in the Raman spectrum of the cycled BESE further confirms this (Figure S27, Supporting Information). Moreover, the ion transport performance of cycled FESE remains significantly superior to that of BESE. These findings fully demonstrate that FESE achieves exceptional structural stability and electrochemical performance due to its excellent fiber network encapsulation structure and selective transmembrane transport mechanism.

3. Conclusion

In summary, we propose a construction strategy of FESE based on the electrospinning-induced phase separation. The FESE features a structure in which an elastomeric layer with Li^+-selective permeability encapsulates a fibrous PCE. The HNBR encapsulation layer in FESE effectively stabilizes and confines the PCE through a quasi-surface-active effect. Benefiting from the interconnected ion transport channels of the PCE phase, the Li^+-selectivity of the HNBR encapsulation layer, and the conformal interface formed by in situ polymerization, the FESE exhibits a high room-temperature ionic conductivity of 1.11 mS cm^{-1} and a Li^+ transference number of 0.77. The as-assembled SSLSB delivers a high initial discharge capacity (1188 mAh g^{-1} at 0.1C with a capacity retention of 78.1%) and remarkable rate capability (356 mAh g^{-1} at 4C). Even under extreme conditions of high loading at 1C, the SSLSB with a sulfur loading of 5.0 mg cm^{-2} maintains a high-capacity retention of 71.2% after 800 cycles. The ingeniously designed phase separation construction strategy and FESE system in this work provide an excellent approach for high-performance solid-state batteries.

Supporting Information

Supporting Information is available from the Wiley Online Library or from the author.

Acknowledgements

The authors greatly appreciated the financial support of the National Natural Science Foundation of China (22478120, 22109045).

Conflict of Interest

The authors declare no conflict of interest.

Data Availability Statement

The data that support the findings of this study are available from the corresponding author upon reasonable request.

Keywords

elastomeric electrolyte, electrospinning, lithium-sulfur batteries, phase separation, plastic crystal

Received: April 17, 2025
Revised: June 9, 2025
Published online:

[1] H. Song, K. Münch, X. Liu, K. Shen, R. Zhang, T. Weintraut, Y. Yusim, D. Jiang, X. Hong, J. Meng, Y. Liu, M. He, Y. Li, P. Henkel, T. Brezesinski, J. Janek, Q. Pang, *Nature* **2025**, *637*, 846.
[2] W. Wang, L. Hua, Y. Zhang, G. Wang, C. Li, *Angew. Chem., Int. Ed.* **2024**, *63*, 202405920.
[3] X. Meng, Y. Liu, Y. Ma, Y. Boyjoo, J. Liu, J. Qiu, Z. Wang, *Adv. Mater.* **2023**, *35*, 202212039.
[4] D. Wang, C. Liu, R. Wang, T. Zhang, B. Chen, T. Wang, Q. Lu, W. Yin, X. Liu, *Angew. Chem., Int. Ed.* **2025**, *64*, 202501411.
[5] D. Wang, L.-J. Jhang, R. Kou, M. Liao, S. Zheng, H. Jiang, P. Shi, G.-X. Li, K. Meng, D. Wang, *Nat. Commun.* **2023**, *14*, 1895.
[6] P. Sayavong, W. Zhang, S. T. Oyakhire, D. T. Boyle, Y. Chen, S. C. Kim, R. A. Vilá, S. E. Holmes, M. S. Kim, S. F. Bent, Z. Bao, Y. Cui, *JACS* **2023**, *145*, 12342.
[7] L.-L. Chiu, S.-H. Chung, *J. Mater. Chem. A* **2022**, *10*, 13719.
[8] S. L. Liu, W. Y. Liu, D. L. Ba, Y. Z. Zhao, Y. H. Ye, Y. Y. Li, J. P. Liu, *Adv. Mater.* **2023**, *35*, 202110423.
[9] Z. Li, J. Fu, X. Zhou, S. Gui, L. Wei, H. Yang, H. Li, X. Guo, *Adv. Sci.* **2023**, *10*, 202201718.
[10] H. Liu, Y. Ye, F. Zhu, X. Zhong, D. Luo, Y. Zhang, W. Deng, G. Zou, H. Hou, X. Ji, *Angew. Chem., Int. Ed.* **2024**, *63*, 202409044.
[11] F. Pei, L. Wu, Y. Zhang, Y. Liao, Q. Kang, Y. Han, H. Zhang, Y. Shen, H. Xu, Z. Li, Y. Huang, *Nat. Commun.* **2024**, *15*, 351.
[12] H. Peng, T. Long, J. Peng, H. Chen, L. Ji, H. Sun, L. Huang, S. G. Sun, *Adv. Energy Mater.* **2024**, *14*, 202400428.
[13] W. Zhang, V. Koverga, S. Liu, J. Zhou, J. Wang, P. Bai, S. Tan, N. K. Dandu, Z. Wang, F. Chen, J. Xia, H. Wan, X. Zhang, H. Yang, B. L. Lucht, A.-M. Li, X.-Q. Yang, E. Hu, S. R. Raghavan, A. T. Ngo, C. Wang, *Nat. Energy* **2024**, *9*, 386.
[14] X. Xie, P. Zhang, X. Li, Z. Wang, X. Qin, M. Shao, L. Zhang, W. Zhou, *JACS* **2024**, *146*, 5940.

[15] S. Han, P. Wen, H. Wang, Y. Zhou, Y. Gu, L. Zhang, Y. Shao-Horn, X. Lin, M. Chen, *Nat. Mater.* **2023**, *22*, 1515.
[16] X. Cai, J. Ding, Z. Chi, W. Wang, D. Wang, G. Wang, *ACS Nano* **2021**, *15*, 20489.
[17] C. Yang, Q. Wu, W. Xie, X. Zhang, A. Brozena, J. Zheng, M. N. Garaga, B. H. Ko, Y. Mao, S. He, Y. Gao, P. Wang, M. Tyagi, F. Jiao, R. Briber, P. Albertus, C. Wang, S. Greenbaum, Y.-Y. Hu, A. Isogai, M. Winter, K. Xu, Y. Qi, L. Hu, *Nature* **2021**, *598*, 590.
[18] P. Shi, J. Ma, M. Liu, S. Guo, Y. Huang, S. Wang, L. Zhang, L. Chen, K. Yang, X. Liu, Y. Li, X. An, D. Zhang, X. Cheng, Q. Li, W. Lv, G. Zhong, Y.-B. He, F. Kang, *Nat. Nanotechnol.* **2023**, *18*, 602.
[19] X. He, Z. Zhu, G. Wen, S. Lv, S. Yang, T. Hu, Z. Cao, Y. Ji, X. Fu, W. Yang, Y. Wang, *Adv. Mater.* **2023**, *36*, 202307599.
[20] L. Hu, J. Wang, K. Wang, Z. Gu, Z. Xi, H. Li, F. Chen, Y. Wang, Z. Li, C. Ma, *Nat. Commun.* **2023**, *14*, 3807.
[21] S. Li, S. J. Yang, G. X. Liu, J. K. Hu, Y. L. Liao, X. L. Wang, R. Wen, H. Yuan, J. Q. Huang, Q. Zhang, *Adv. Mater.* **2023**, *36*, 202307768.
[22] J.-C. Wang, L.-L. Zhao, N. Zhang, P.-F. Wang, T.-F. Yi, *Nano Energy* **2024**, *123*, 109361.
[23] S. Kalnaus, N. J. Dudney, A. S. Westover, E. Herbert, S. Hackney, *Science* **2023**, *381*, abg5998.
[24] J. Shao, Y. Li, J. Guo, J. Duan, H. Liang, Y. Dou, S. Lu, J. Liu, *Adv. Mater.* **2025**, https://doi.org/10.1002/adma.202415864.
[25] H. Kloppenburg, T. Groß, M. Mezger, C. Wrana, *Chem. unserer Zeit* **2009**, *43*, 392.
[26] M. J. Lee, J. Han, K. Lee, Y. J. Lee, B. G. Kim, K.-N. Jung, B. J. Kim, S. W. Lee, *Nature* **2022**, *601*, 217.
[27] M. Li, Z. Huang, Y. Liang, Z. Wu, H. Zhang, H. Chen, S. Zhang, *Adv. Funct. Mater.* **2024**, *35*, 202413580.
[28] J. Zhang, H. Wu, X. Du, H. Zhang, L. Huang, F. Sun, T. Liu, S. Tian, L. Zhou, S. Hu, Z. Yuan, B. Zhang, J. Zhang, G. Cui, *Adv. Energy Mater.* **2022**, *13*, 202202529.
[29] T. Weigel, G. Schinkel, A. Lendlein, *Expert Rev. Med. Devices* **2014**, *3*, 835.
[30] T.-C. Chan, S.-H. Chung, *ACS Sustainable Chem. Eng.* **2024**, *12*, 14230.
[31] H. Xiao, Y. Song, G. Chen, *J. Electrostat.* **2014**, *72*, 311.
[32] W. Li, J. Hao, P. Zhou, Y. Liu, C. Lu, Z. Zhang, *J. Appl. Polym. Sci.* **2017**, *134*, 45405.
[33] P. Q. Yao, Q. W. Bao, Y. Yao, M. Xiao, Z. Y. Xu, J. H. Yang, W. G. Liu, *Adv. Mater.* **2023**, *35*, 202300114.
[34] X. Zhang, W. P. Xiong, T. Wang, E. R. Chai, J. Lin, L. T. Huang, Y. Y. Feng, M. X. Wu, Y. B. Wang, *Nat. Catal.* **2024**, *7*, 55.
[35] C. Zhang, H. Liang, D. Liang, Z. Lin, Q. Chen, P. Feng, Q. Wang, *Angew. Chem., Int. Ed.* **2020**, *60*, 4289.
[36] H.-M. Wang, M. Geng, J. Bai, D. Zhou, W. Hua, S. Liu, X. Gao, *Mater. Horiz.* **2025**, *12*, 141.
[37] J. Yang, Y. Chu, X. Zhang, Y. Li, X. Cui, Q. Pan, *J. Storage Mater.* **2024**, *96*, 112539.
[38] K. Liu, H. Cheng, Z. Wang, Y. Zhao, Y. Lv, L. Shi, X. Cai, Z. Cheng, H. Zhang, S. Yuan, *Adv. Energy Mater.* **2024**, *14*, 202303940.
[39] D. Cao, X. Sun, F. Li, S. M. Bak, T. Ji, M. Geiwitz, K. S. Burch, Y. Du, G. Yang, H. Zhu, *Angew. Chem., Int. Ed.* **2023**, *62*, 202302363.
[40] R. Elizalde-Segovia, A. Irshad, B. Zayat, S. R. Narayanan, *J. Electrochem. Soc.* **2020**, *167*, 140529.